Inorganic Chemistry

Article

pubs.acs.org/IC

A Ligand Field Series for the 4f-Block from Experimental and DFT Computed Ce(IV/III) Electrochemical Potentials

Justin A. Bogart,[†] Andrew J. Lewis,[†] Michael A. Boreen,[†] Heui Beom Lee,[†] Scott A. Medling,[‡] Patrick J. Carroll,[†] Corwin H. Booth,[‡] and Eric J. Schelter*[,†]

[†]P. Roy and Diana T. Vagelos Laboratories, Department of Chemistry, University of Pennsylvania, Philadelphia, Pennsylvania 19104, United States

[‡]Chemical Sciences Division, Lawrence Berkeley National Laboratory, Berkeley, California 94720, United States

Supporting Information

ABSTRACT: Understanding of the sensitivity of the reduction potential of cerium(IV) cations to ligand field strength has yet to benefit from systematic variation of the ligand environment. Detailed analyses for a series of seven cerium(IV) tetrakis(pyridyl-nitroxide) compounds and their cerium(III) analogues in varying ligand field strengths are presented. Electrochemical, spectroscopic, and computational results reveal a close correlation of electronic properties with ligand substituents. Together with electrochemical data for reported eight-coordinate compounds, DFT calculations reveal a broad range of the cerium(IV/III) redox potentials correlated to ligand field strengths, establishing a semiempirical, predictive model for the modulation of cerium redox thermodynamics and ligand field strengths. Applications over a variety of scientific disciplines make use of the fundamental redox thermodynamics of cerium. Such applications will benefit from a combined experimental and theoretical approach for assessing redox cycling of cerium compounds.

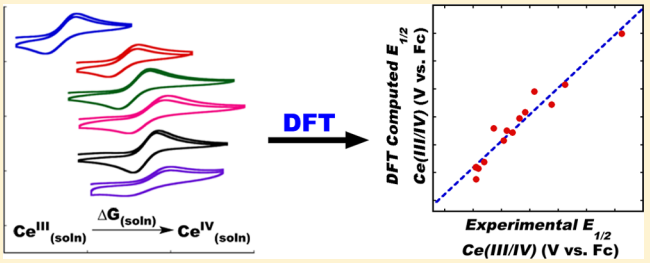

INTRODUCTION

Cerium is a unique member of the lanthanide series with an accessible molecular chemistry in both the tetravalent and trivalent oxidation states.[1] The rich redox chemistry that results from the accessibility of the tetravalent oxidation state has found use in many applications. Due to the chemical reversibility of the Ce_2O_3/CeO_2 redox cycle, for example, CeO_2 can be used as an active support in 3-way catalytic converters to both store and provide oxygen equivalents for the oxidation of CO to CO_2.[2] The redox properties of nanoceria are also used in medicinal chemistry, where CeO_2 nanoparticles have been proposed as radical scrubbers for the treatment of ischemic stroke.[3] Ceric ammonium nitrate (CAN) is widely used in synthetic chemistry as a potent oxidant for the oxidation of alcohols to carbonyls.[4] CAN also finds use in energy science as a terminal oxidant in the catalytic oxidation of water. In such cases, 4 equiv of CAN accept the four electrons needed to oxidize two molecules of H_2O to O_2.[5,6]

Recently, we provided evidence that hydroxamate collectors used in the beneficiation of light rare earth ores induce oxidation of cerium at ore particle surfaces, implying collector efficiency is related to cerium redox chemistry.[7] Similarly, separations of cerium from rare earth concentrates also benefit from cerium(IV/III) redox chemistry. Roasting of the rare-earth mixture oxidizes Ce_2O_3 to CeO_2, which prevents leaching of cerium into the dilute HCl solution.[8,9] In these cases and many others, cerium redox chemistry plays a pivotal role. In this context, there is a clear need to develop predictive methods for cerium(IV/III) redox chemistry across a wide variety of compounds and ligand environments.

Toward this goal, we devoted effort to understanding the relationship between crystal field strength and cerium redox chemistry and explored whether this relationship could be modeled computationally. In a survey of reported electrochemical potentials, we established that the cerium(IV/III) redox couple is highly sensitive to its ligand environment, spanning a range of over 2 V under either aqueous or nonaqueous conditions.[10] In work on the modeling of the active site of the recently discovered, rare earth dependent XoxF-type methanol dehydrogenase, we successfully used DFT methods on four model cerium complexes to create a correlation between calculated and experimental aqueous redox potentials.[11] These results provided proof of concept that we could successfully unite cerium redox chemistry with quantum chemistry probes.

In this Article, we set out to construct a more extensive correlation of crystal fields with cerium redox potentials under nonaqueous conditions. As an initial step, we sought to expand on our previous work with cerium pyridyl-nitroxide chemistry.[12] The goals of these efforts were to develop a series of compounds within a conserved ligand framework where ligand substituent effects could be used to probe the sensitivity of the cerium(IV/III) redox couple. A secondary goal was to identify

Received: December 16, 2014
Published: February 24, 2015

DOI: 10.1021/ic503000z
Inorg. Chem. 2015, 54, 2830−2837

the most reducing cerium(III) complexes possible to establish a wide range of potentials. We expected the results of these efforts would form the basis of our correlation of DFT with electrochemistry.

In the current work, we have prepared a series of structurally related complexes of the general formulae $[Ce^{III}(\mu\text{-}(R\text{-}2\text{-}(^t\text{BuNO})py))(R\text{-}2\text{-}(^t\text{BuNO})py)_2]_2$ (**1-X**) and $Ce^{IV}[R\text{-}2\text{-}(^t\text{BuNO})py]_4$ (**2-X**), where R = 5-CF_3 (**1-CF$_3$**, **2-CF$_3$**), 5-Me (**1-Me**, **2-Me**), 3-OMe (**1-OMe**, **2-OMe**), 5-NMe_2 (**1-*p*NMe$_2$**, **2-*p*NMe$_2$**), and 4-NMe_2 (**1-*m*NMe$_2$**, **2-*m*NMe$_2$**) (Figure 1).

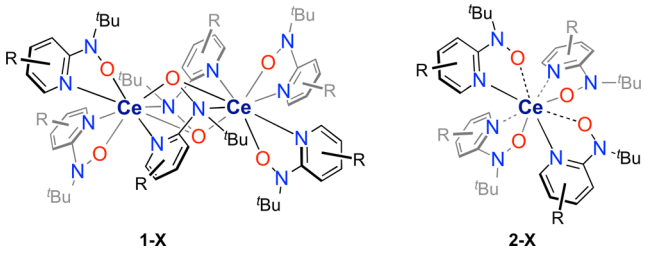

Figure 1. Generic structures of **1-X** (left) and **2-X** (right), where X = -CF_3, -H, -Me, -OMe, -*p*NMe_2, and -*m*NMe_2 complexes. Note that the **2-OMe** structure has approximate S_4 symmetry rather than approximate D_{2d} symmetry.

Solution electrochemistry experiments indicated a shift in the potential of the $Ce^{IV/III}$ redox event of 500 mV over the series. These results were corroborated by DFT B3LYP calculations, in which the redox potentials were correlated with calculated $E_{1/2}$ Ce(IV/III) values. We expanded this correlation to include nine cerium compounds from the literature. Overall, these results comprise a new method for organizing donor types into a ligand field series for cerium; they are important steps in using combined quantum chemistry and experimental approaches to understand and predict redox chemistry of cerium in novel ligand environments.

RESULTS

Synthesis of $Ce^{IV}[R\text{-}2\text{-}(^t\text{BuNO})py]_4$ Complexes. Following our reported synthesis of the cerium pyridyl-nitroxide complex $Ce^{IV}[2\text{-}(^t\text{BuNO})py]_4$,[12] we synthesized analogues of the dimeric $[Ce^{III}(\mu\text{-}(2\text{-}(^t\text{BuNO})py))(2\text{-}(^t\text{BuNO})py)_2]_2$ complex with a series of substituted pyridyl hydroxylamines, R-2-(^{t}BuNOH)py, where R = 5-CF_3, 5-Me, 3-OMe, 5-NMe_2, and 4-NMe_2. Layering or gently mixing 1 equiv of $Ce[N(SiMe_3)_2]_3$ with 3 equiv of R-2-(^{t}BuNOH)py[13] led to the deposition of X-ray quality crystals, which confirmed the dimeric structures. These dimeric Ce^{III} complexes, **1-X**, were oxidized to the desired $Ce^{IV}[R\text{-}2\text{-}(^t\text{BuNO})py]_4$ products, **2-X**, upon reaction with 2 equiv of neutral R-2-(^{t}BuNO)py nitroxide radical, formed in situ from the oxidation of R-2-(^{t}BuNOH)py with excess PbO_2 (Figure 1).

The **1-X** dimers were stable under a nitrogen atmosphere without the addition of an external oxidant. However, even without the addition of ligand, the Ce^{III} dimers would convert to their monomeric Ce^{IV} congeners upon oxidation through ligand redistribution pathways. Therefore, for the ensuing electrochemistry and computational studies, we focused on the series of **2-X** Ce^{IV} complexes to ensure conserved ligand environments throughout the redox cycles.

X-ray Structural Analysis. Complexes **1-CF$_3$**, **1**, **1-Me**, **1-OMe**, **1-*m*NMe$_2$**, and **1-*p*NMe$_2$** were isostructural in the solid state as indicated by the similarities in structural metrics shown in Table S1 in the Supporting Information. X-ray analysis of **2-CF$_3$**, **2**, **2-Me**, **2-*p*NMe$_2$**, and **2-*m*NMe$_2$** revealed a conserved coordination environment with approximate D_{2d} symmetry. The geometry of **2-OMe** differed from the others, exhibiting approximate S_4 symmetry (Figure S1 in the Supporting Information). DFT calculations on optimized structures of complex **2-OMe** in approximate D_{2d} and S_4 symmetry indicated that there was negligible difference in energy between the two geometries (*vide infra*).

It was evident from the crystal structure of complex **2-OMe** that the ^{t}BuNO moieties were significantly pyramidalized at the nitrogen atom as well as rotated out of plane with the pyridyl ring compared to the structure of complex **2-CF$_3$** in which the ^{t}BuNO groups were coplanar with the pyridine ring (Figure 2).

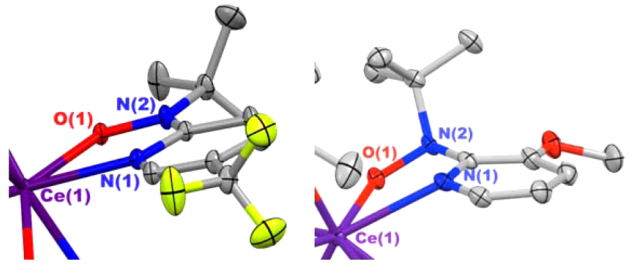

Figure 2. Partial thermal ellipsoid plots of **2-CF$_3$** (left) and **2-OMe** (right) indicating the relative increase in pyramidalization by comparison at N(2).

The degree of out of plane rotation was assessed by averaging the $N_{pyr}\text{–}C\text{–}N^t_{BuNO}\text{–}C$ torsion angles, and the average of the sums of the angles about the hydroxylamine nitrogen atoms ($\sum Y\text{–}N^t_{BuNO}\text{–}Z$) was used to assess the degree of pyramidalization. These angles as well as selected bond distances for the series of Ce^{IV} complexes are listed in Table 1.

The interplanar torsion angles increased from 2.51° for complex **2-CF$_3$** to 66.15° for complex **2-OMe**. This increase correlated with the electron donating ability of the substituents on the pyridyl rings into the ^{t}BuNO moieties. A similar trend was observed with the degree of pyramidalization, which decreased from 359.9(2)° in complex **2-CF$_3$** to 337.17(15)° in complex **2-*p*NMe$_2$**. On the basis of the Hammett parameters for substituents in the para position ($\sigma_p^+ = -0.78$ for OMe and -1.70 for NMe_2),[14] we expected the degree of rotation in complex **2-*p*NMe$_2$** to be greater than that in complex **2-OMe**. The unexpected smaller torsion angles observed in the solid state structure of **2-*p*NMe$_2$** (Table 1) were attributed to steric repulsion from the larger *o*-OMe group that was increased in the former relative to the *o*-H group in the latter.

Electronic Absorption and XAS Spectroscopies. All of the **2-X** monomeric complexes exhibited characteristic intense, dark red to dark purple colors. Ce^{IV} complexes typically exhibit intense colors due to allowed ligand-to-metal charge transfer (LMCT) transitions. These LMCT transitions span a range of wavelengths depending on the ligand environment.[15] The electronic absorption spectra revealed a set of two broad transitions in all of the complexes except **2-*m*NMe$_2$**, which only showed the lower energy transition (Figure 3). The lower energy transition was previously assigned as LMCT.[12]

To definitively assign the electronic transitions, we prepared the complex $[K(18\text{-crown-}6)(py)_2][La(2\text{-}(^t\text{BuNO})py)_4]$ (**3**) through a similar route to the analogous cerium(III) complex.[12] In this context, transitions that have metal character, such as

DOI: 10.1021/ic503000z
Inorg. Chem. 2015, 54, 2830−2837

Table 1. Experimental and Computational Structural Metrics

	N−O (Å)		Ce−O (Å)		Ce−N_{pyr} (Å)		∑Y−N^{t}_{BuNO}−Z angles (deg)	N_{pyr}−C−N^{t}_{BuNO}−C torsion angles (deg)
	exp.	calc.	exp.	calc.	exp.	calc.	exp.	exp.
2-CF_3	1.368(2)	1.367	2.2318(14)	2.247	2.5416(16)	2.625	359.9(2)	2.51
2	1.375(2)	1.370	2.2356(13)	2.247	2.5434(17)	2.639	358.6(2)	7.49
2-Me	1.392(3)	1.390	2.2201(18)	2.224	2.566(2)	2.658	348.7(2)	29.65
2-OMe (S_4)	1.410(6)	1.398	2.193(4)	2.210	2.633(4)	2.725	337.9(7)	66.15
2-OMe (D_{2d})		1.381		2.235		2.664		
2-*p*NMe_2	1.4092(17)	1.395	2.2039(10)	2.224	2.5829(14)	2.675	337.17(15)	49.17
2-*m*NMe_2	1.399(2)	1.378	2.2269(14)	2.250	2.5415(17)	2.633	349.39(19)	29.23

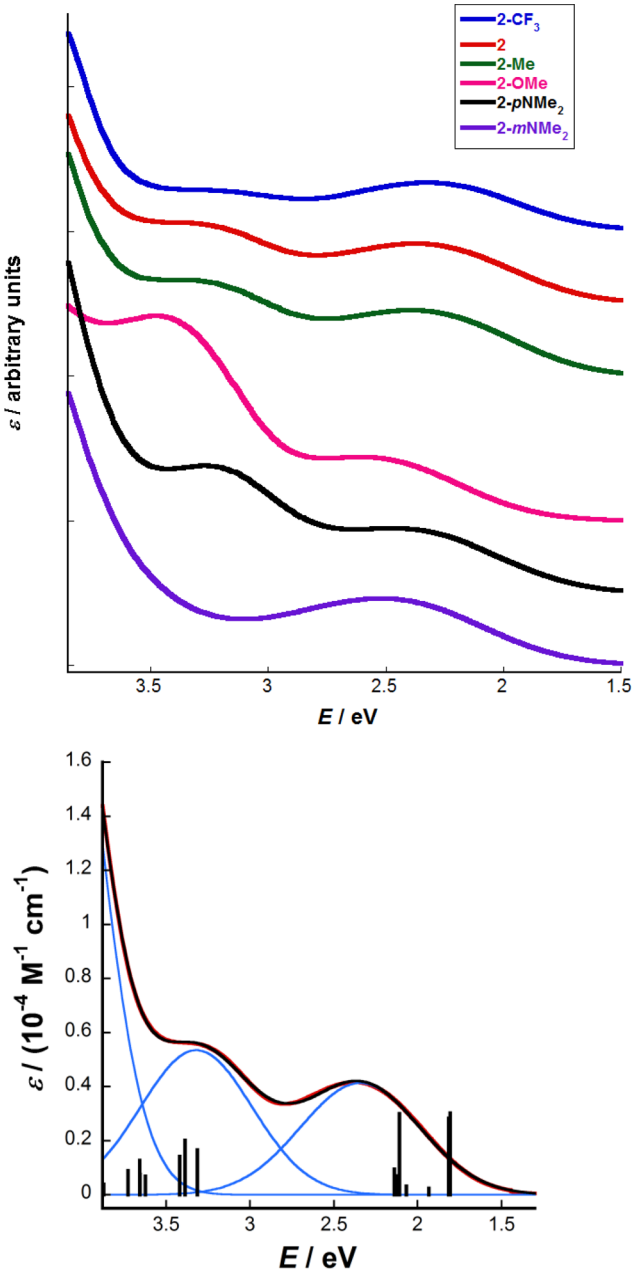

Figure 3. Experimental electronic absorption spectra for the **2-X** complexes (top) and TD-DFT calculated excitation profile for **2** (bottom).

LMCT, would occur at significantly different energies within complexes **2** and **3**. The UV−vis spectrum of **3** displayed a single broad absorption at 3.08 eV. The absence of a second broad band provided further support for assignment of the 2.0−2.5 eV bands of **2-X** as LMCT. On this basis, we could also assign the higher energy of the two features in **2-X** as excitations localized on the pyridyl nitroxide ligand.

To corroborate the UV−vis band assignments, we turned to TD-DFT, a method that has been used successfully to predict the absorption spectra of lanthanide complexes.[16] Representative TD-DFT calculations incorporating acetonitrile solvation revealed vertical excitations at 2.07 eV for **2** and 2.16 eV for **2-CF_3**, characterized as transitions from an occupied nitroxide π^* orbital to vacant cerium 4f orbitals, indicating LMCT character. TD-DFT also supported the nature of the higher energy feature as a ligand-based nitroxide π^* to pyridyl π^* excitation for those complexes with the higher energy bands (see Supporting Information).

Cerium(IV) compounds are known to exhibit valence instability;[17] multiconfigurational ground states have been previously observed for organo-cerium(IV) compounds bearing redox non-innocent ligands.[18,19] Such phenomena arise from the mixing of electronic states that reflect transfer of electrons from low-lying ligand π^* orbitals to energetically close metal 4f acceptor orbitals. In such cases, low energy LMCT bands are visible in the electronic absorption spectrum.[20] The canonical multiconfigurational organocerium compound is cerocene: $Ce(COT)_2$, where COT = cyclooctatetraene;[19,21] the lowest energy, formally LMCT band for cerocene was reported at 2.18 eV.[22] To study the possibility of multiconfigurational ground states in the **2-X** complexes, we performed Ce L_{III} edge X-ray absorption spectroscopy on **1-X** and **2-X**, X = -CF_3 and -*p*NMe_2 congeners, for comparison to the data reported by us for **1** and **2** (Figure 4).[12] In all cases, the data for the cerium(III) **1-X** compounds revealed single white line absorbance at energies consistent with cerium(III) cations. For the **2-X** compounds, the data revealed two absorption features, consistent with core hole excitation of the Ce^{IV} ion, such as in $Ce^{IV}[2\text{-}(^{t}BuNO)py]_4$.[12] In this case, the pair of transitions correspond to the final states $2p4f^{1}\underline{L}5d^{1}$ and $2p4f^{0}5d^{1}$, where $\underline{L}$ indicates a ligand hole and the f^1 contribution indicates the degree of covalency.[20] The data were essentially identical to those recorded for **2** and support assignment of both **2-CF_3** and **2-*p*NMe_2** as true cerium(IV) complexes, indicating that tuning the ligand redox potential by ∼500 mV for this system does not introduce multiconfigurational character to the resulting cerium(IV) complexes. Having established the true valence electronic structure across the series, we next examined the purely metal-based electrochemistry of the compounds.

Solution Electrochemistry. The relative stabilization of the tetravalent oxidation state for the series of functional

DOI: 10.1021/ic503000z
Inorg. Chem. 2015, 54, 2830−2837

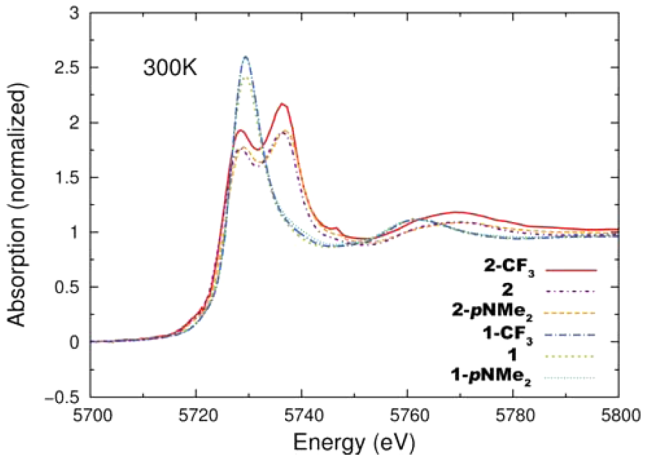

Figure 4. Ce L_{III} edge XAS data for the cerium(III) compounds **1**, **1-CF$_3$**, and **1-*p*NMe$_2$** and their cerium(IV) congeners **2**, **2-CF$_3$**, and **2-*p*NMe$_2$**.

derivatives of **2** was assessed using the potentials of the $Ce^{IV/III}$ redox couple observed in solution electrochemistry experiments (Figure 5). These experiments were performed in a 0.1 M [^{n}Pr$_4$N][BAr$^F_4$] THF/MeCN (1:4) solution, BAr$^F_4$ = B(3,5-(CF$_3$)$_2$-C$_6$H$_3$)$_4$, as these conditions yielded the smallest anodic (E_{pa}) to cathodic (E_{pc}) wave separation for the quasi-reversible $Ce^{IV/III}$ redox couples (see Supporting Information). The addition of THF was necessary to dissolve the complexes, which were only slightly soluble in neat MeCN solutions. The $E_{1/2}$ values obtained from these experiments are listed in Table 2.

As expected, the potential of the $Ce^{IV/III}$ redox event shifted to more negative potentials with the more electron-rich pyridyl-nitroxide ligands coordinated to the central cerium cation. We were surprised, however, that despite the increasing substituent donating ability from -Me to -OMe to -*p*-NMe$_2$, there was not a significant shift in the reduction potential of Ce in the respective complexes (Table 2, Figure 5). We previously observed a linear dependence of redox potentials on substituent donating abilities in the solution electrochemistry of the radical to oxo-ammonium $E_{1/2}$ for the nitroxide ligands alone.[13] We attributed this smaller than expected substituent effect in these complexes to pyramidalization and rotation of the nitroxide moieties, which reduced conjugation with the pyridyl π system. As such, electron donating substituents beyond -Me showed a negligible effect on cerium oxidation potential due to the inferred electronic feedback/distortion of the nitroxide-pyridyl ring system, as observed in a plot of DFT-computed ligand redox properties versus the experimental Ce(IV/III) reduction potentials of the **2-X** complexes (Figure 5). We next turned to solution phase DFT calculations to further corroborate these experimental observations.

DFT Studies. The electronic structure of the series of cerium(IV) **2-X** complexes was explored through solution DFT methods, revealing systematic variation in the frontier molecular orbitals (see Supporting Information). Notably, the LUMO through LUMO+6 virtual orbitals of predominantly Ce 4f character exhibited a trend of destabilization directly related to the experimentally observed $Ce^{IV/III}$ reduction potential. In fact, a linear correlation was established between the calculated energy of the LUMO and the experimentally determined $Ce^{IV/III}$ redox potentials (Figure 6). Ephritikhine and co-workers previously found good correlation between computed

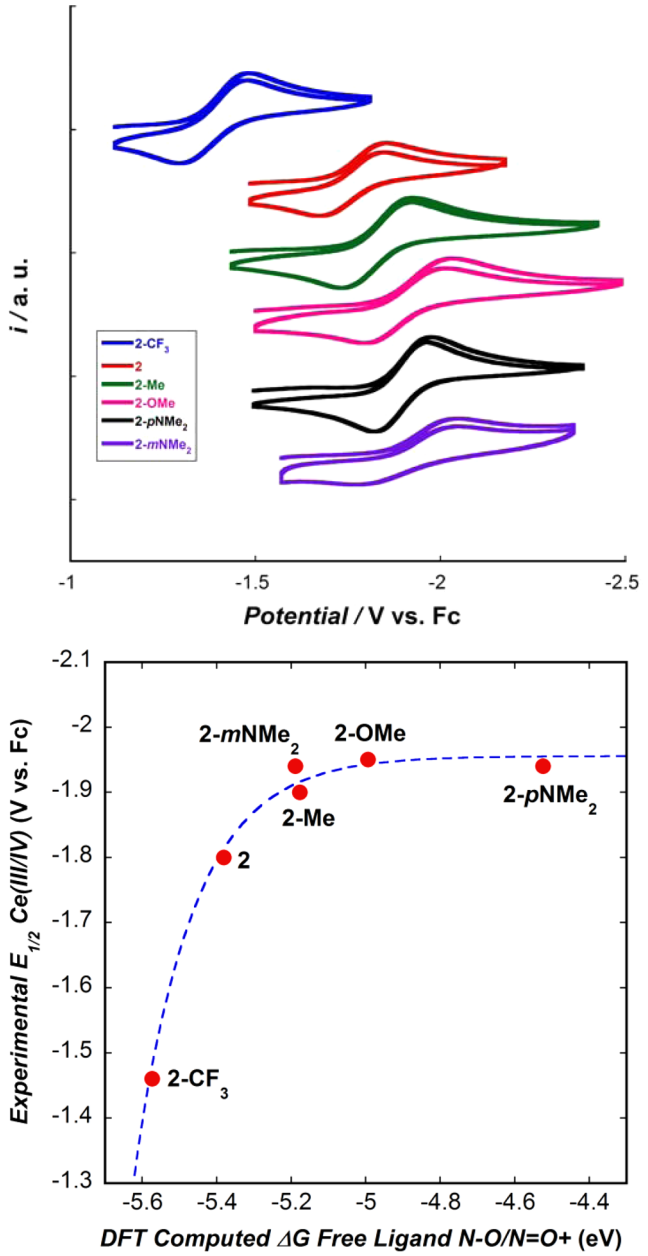

Figure 5. Cyclic voltammograms of the isolated $Ce^{IV/III}$ reduction features in the **2-X** complexes (top) and correlation between metal redox potentials in the **2-X** complexes and DFT computed free energy changes for the free ligand N−O/N═O$^+$ redox event (bottom).

electron affinities and $E_{1/2}$ uranium(IV/III) reduction potentials across a range of ∼275 mV for five compounds,[27] though the **2-X** series spans a wider range of $E_{1/2}$ cerium(IV/III) reduction potentials.

In addition to the computations on the cerium(IV) complexes **2-X**, unrestricted B3LYP DFT calculations on isostructural anionic complexes with cerium in the 3+ oxidation state were performed to calculate the $E_{1/2}$ $Ce^{IV/III}$ values (see Supporting Information).[28] For guidance in these calculations, we used the structurally characterized [K(18-crown-6)py$_2$][Ce-(2-(^{t}BuNO)py]$_4$ complex,[12] which constituted a reduced form of **2**, as a point of reference. The solvated cerium(III) optimization completed the thermochemical cycle needed to correlate with the observed $E_{1/2}$ values (Scheme 1).

DOI: 10.1021/ic503000z
Inorg. Chem. 2015, 54, 2830−2837

Table 2. Calculated and Experimental Electrochemical Data

	$E_{1/2}$ (V vs Fc)		
	exp.	calc.[a]	ref.
2-CF_3	−1.46	−1.43	this work
2	−1.80	−1.81	this work
2-Me	−1.90	−1.93	this work
2-OMe	−1.95	−1.91	this work
2-*p*NMe_2	−1.94	−1.90	this work
2-*m*NMe_2	−1.94	−2.12	this work
$[^nBu_4N]_2[Ce(NO_3)_6]$	+0.62	+0.49	23
$Ce(acac)_2$[b]	−0.38	−0.42	24
$Ce(BrSALEN)_2$[c]	−0.92	−0.55	25
$Ce(SALEN)_2$	−1.08	−0.92	25
$Ce(OMeSALEN)_2$	−1.18	−1.03	25
$Ce(OQ)_2$[d]	−0.61	−0.78	this work
$Ce(HA)_4$[e]	−1.30	−1.28	7
$Ce(C_8H_8)_2$	−1.40	−1.25	26
$Ce(omtaa)_2$[f]	−1.63	−1.21	this work
MAD[g]		−0.13	

[a]All potentials were adjusted by 0.30 mV to account for systematic error. [b]acac = acetylacetonate. [c]SALEN = 2,2′-ethylenebis-(nitrilomethylidene)diphenol. [d]OQ = 8-hydroxyquinolinate. [e]HA = *N*-phenyl-pivalohydroxamate. [f]omtaa = octamethyltetraazaanulene. [g]MAD = mean absolute deviation.

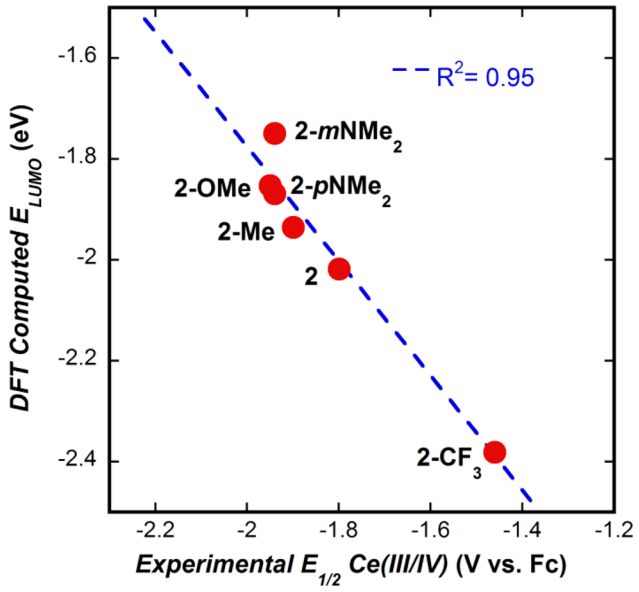

Figure 6. Correlation between LUMO energy and reduction potential.

Scheme 1. Thermodynamic Cycle Used for the Calculation of $\Delta G_{(soln)}$ between the Ce^{III} and Ce^{IV} States

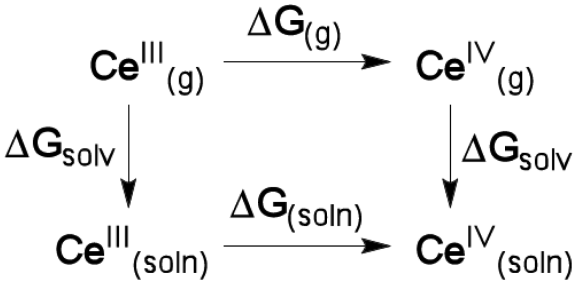

Whereas Batista and co-workers effectively correlated $E_{1/2}$ values to single point computed 3/4/5d transition metal structures,[29] complete geometry optimizations were performed in all cases for **2-X** and $[\mathbf{2\text{-}X}]^-$ here. After an empirical correction factor of 0.30 V was applied to the calculated $E_{1/2}$ values to account for systematic errors arising from the use of ferrocene as a reference for Ce complexes, these DFT-computed redox potentials correlated well with experimental values (Figure 7). It is also noteworthy that Batista and co-

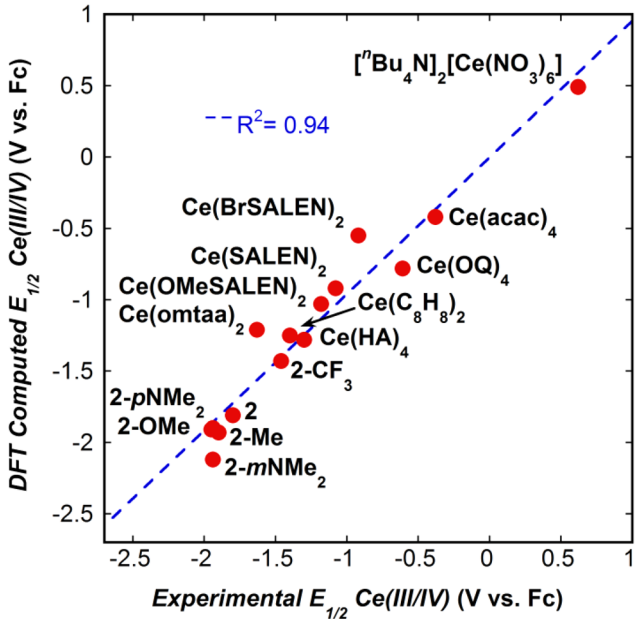

Figure 7. Correlation between calculated and experimental $Ce^{IV/III}$ reduction potentials.

workers observed systematic errors in their calculations when ferrocene was used as a reference for the second or third row transition metal complexes.[29] Thus, the combined X-ray structural, electrochemical, and DFT analyses were validated for our series of six pyridyl-nitroxide **2-X** complexes, spanning an $E_{1/2}$ range of ∼500 mV.

Following our success with the **2-X** series, we were interested in applying the approach more broadly to cerium compounds in general. As a limiting factor, we examined complexes with similar coordination geometries but varying ligand field strengths. A natural extension was to cerium hydroxamate complexes. Hydroxamates are key agents in the froth flotation separation unit operations for the isolation of lanthanides from their ores,[30,31] creating a broad interest in the ability to predict their ligand field strengths through simple calculations. Furthermore, the crystal structure of the $Ce(HA)_4$ complex (where HA = *N*-phenyl-pivalohydroxamate) recently reported by us revealed a similar D_{2d} geometry.[7] On the basis of our reported electrochemistry of this complex, however, the hydroxamate ligands imposed a ligand field around the central cerium cation that was weaker than that of the pyridyl-nitroxide system. The calculated $Ce^{IV/III}$ redox potential of −1.28 V for $Ce(HA)_4$ was within 20 mV of the experimentally determined $E_{1/2}$ value as estimated by averaging the anodic and cathodic wave potentials in the cyclic voltammogram.

We also examined the aryl oxide ligand frameworks in the reported $Ce(OMeSALEN)_2$, $Ce(SALEN)_2$, $Ce(BrSALEN)_2$, and $Ce(OQ)_4$ (OQ = 8-hydroxyquinolinate) complexes, as well

DOI: 10.1021/ic503000z
Inorg. Chem. 2015, 54, 2830−2837

as the carbon-based framework of COT^{2-} in cerocene, the oxygen-based framework of $acac^-$ in $Ce(acac)_4$, and the nitrogen-based framework of $omtaa^{2-}$ in $Ce(omtaa)_2$ for comparison.[24−26,32,33] Again, the DFT computed $E_{1/2}$ $Ce^{IV/III}$ values matched well with the experimental values.

Finally, we examined whether the redox potential of $[^nBu_4N]_2[Ce(NO_3)_6]$ could be predicted despite the different geometry imposed by the six bidentate nitrate ligands.[23] The counterions, two $[Et_4N]^+$ groups, were included in the calculations to account for ion pairing effects with the highly charged $[Ce(NO_3)_6]^{2-}$ unit. The ^{n}Bu groups were reduced to Et groups to simplify the calculations. The compound $[^nBu_4N]_2[Ce(NO_3)_6]$ also fit the correlation very well, lending credence to the predictive power of this method over a range >2.5 V.

CONCLUSIONS

In summary, functionalization of the pyridyl group of the 2-(^{t}BuNO)py ligand with electron-withdrawing and -donating groups provided an ∼500 mV range in tuning of the reduction potential of homoleptic cerium(IV) complexes. DFT calculations successfully reproduced the trend in experimental $Ce^{IV/III}$ reduction potentials, which were extended to eight other 8-coordinate cerium complexes as well as CAN. This approach establishes the predictive power of simple DFT methods to unknown cerium redox chemistry. An advantage of our approach is that we use cyclic voltammetry together with X-ray structural data and DFT, techniques that are readily available to many chemists.

We also expect that establishing a ligand field series for cerium will contribute to diverse areas of interest for the element where charge distribution, and potentially its effect on 4f orbital energies through crystal electric fields, plays a critical role, ranging from molecular magnetism[34] to Lewis acid catalysis,[35] reduction chemistry mimicking samarium(II) reagents,[36] and the design of MRI contrast agents.[37,38]

METHODS

General Methods. Unless otherwise noted, all reactions and manipulations were performed under an inert atmosphere (N_2) using standard Schlenk techniques or in a Vacuum Atmospheres, Inc. Nexus II drybox equipped with a molecular sieves 13X/Q5 Cu-0226S catalyst purifier system. Glassware was oven-dried for at least 3 h at 150 °C prior to use. ^{1}H and ^{13}C NMR spectra were obtained on a Bruker DMX-300 Fourier transform NMR spectrometer at 300 and 75.4 MHz, respectively, or a Bruker DRX-500 Fourier transform NMR spectrometer at 500 and 125.6 MHz, respectively. Chemical shifts were recorded in units of parts per million downfield from residual solvent signals. ^{19}F NMR spectra were obtained on a Bruker DRX-500 Fourier transform NMR spectrometer at 282.2 MHz with chemical shifts recorded in units of parts per million relative to an external $CFCl_3$ reference (0 ppm).

X-ray Crystallography. X-ray intensity data were collected on a Bruker APEXII CCD area detector employing graphite-monochromated Mo Kα radiation (λ = 0.71073 Å) at a temperature of 143(1) K. In all cases, rotation frames were integrated using SAINT,[40] producing a listing of unaveraged F^2 and $\sigma(F^2)$ values that were then passed to the SHELXTL[41] program package for further processing and structure solution on a Dell Pentium 4 computer. The intensity data were corrected for Lorentz and polarization effects and for absorption using TWINABS[42] or SADABS.[43] The structures were solved by direct methods (SHELXS-97).[44] Refinement was by full-matrix least-squares based on F^2 using SHELXL-97.[44] All reflections were used during refinements. Non-hydrogen atoms were refined anisotropically and hydrogen atoms were refined using a riding model.

Electrochemistry. Cyclic voltammetry experiments were performed using a CH Instruments 620D electrochemical analyzer/workstation, and the data were processed using CHI software v 9.24. All experiments were performed in an N_2 atmosphere drybox using electrochemical cells that consisted of a 4 mL vial, glassy carbon (3 mm diameter) working electrode, platinum wire counter electrode, and silver wire plated with AgCl as a quasi-reference electrode. The working electrode surfaces were polished prior to each set of experiments and were periodically replaced upon scanning >0 V versus ferrocene (Fc) to prevent the buildup of oxidized product on the electrode surfaces. Potentials were reported versus Fc, which was added as an internal standard for calibration at the end of each run. Solutions employed during CV studies were ∼3 mM in analyte and 100 mM in $[^nPr_4N][B(3,5\text{-}(CF_3)_2\text{-}C_6H_3)_4]$ ($[^nPr_4N][BAr^F{}_4]$). The complexes were measured in 1:4 THF/CH_3CN mixtures. The THF was necessary to dissolve the complexes in solution. The electrochemistry of $Ce(OQ)_4$ was measured in CH_3CN, together with several drops of pyridine in order to dissolve the complex. All data were collected in a positive-feedback IR compensation mode. The solution cell resistances were measured prior to each run to ensure resistances less than or equal to ∼500 Ω.[39] Scan rate dependences of 50−1000 mV/s were performed to determine electrochemical reversibility.

UV−vis Absorption Spectroscopy. All UV−vis absorption measurements were performed using a PerkinElmer 950 UV−vis/NIR spectrophotometer. One mm path length screw cap quartz cells were used with a blank measured before each run.

X-ray Absorption Spectroscopy. Ce L_{III} edge XANES data were collected at the Stanford Synchrotron Radiation Lightsource, beamline 11-2, using a Si 220 (phi = 0) double monochromator that was detuned to 20% to reduce harmonic contamination. The resulting data have an energy resolution limited by the broadening due to the $2p_{3/2}$ corehole lifetime of 3.2 eV. Data were collected in transmission, using a CeO_2 reference to calibrate the energy scale, setting the first inflection point of the CeO_2 absorption to 5723 eV. A linear pre-edge background was subtracted, and the data were subsequently normalized at 5800 eV.

The samples were prepared for these experiments using procedures outlined previously.[45] In particular, each sample was ground into a powder, mixed with dry boron nitride as a diluent, and then packed into the slots of a machined aluminum sample holder in an N_2 atmosphere drybox. Aluminized mylar was affixed to the holder with an indium-wire seal. After packaging, the samples were transported in dry, nitrogen-filled containers to the beamline. Sample holders were quickly transferred to the vacuum chamber, exposing the sealed holders to air for less than 30 seconds before pumping out the chamber and collecting the data under vacuum. Compounds **1-X**, where X = -CF_3, -H, and -pNMe_2, show extreme air sensitivity and have easily identifiable spectral changes upon exposure. These samples served as "canary" samples and were monitored to check for sample holder integrity. Following the measurements, no significant changes in those samples were observed.

MATERIALS

Tetrahydrofuran, dimethoxyethane, diethyl ether, dichloromethane, toluene, hexanes, and pentane were purchased from Fisher Scientific. The solvents were sparged for 20 min with dry N_2 and dried using a commercial two-column solvent purification system comprising columns packed with Q5 reactant and neutral alumina (for hexanes and pentane) or two columns of neutral alumina (for THF, Et_2O, toluene, DME, and CH_2Cl_2). Deuterated solvents were purchased from Cambridge Isotope Laboratories, Inc. and stored over a potassium mirror overnight prior to use. Anhydrous cerium(III) chloride (Strem Chemicals Inc.) was used as received. 2-Bromopyridine (Acros Organics) was degassed using three freeze−pump−thaw cycles and stored for 24 h over 3 Å molecular sieves prior to use. Isopropyl magnesium chloride lithium chloride solution (1.3 M in THF) was purchased from

DOI: 10.1021/ic503000z
Inorg. Chem. 2015, 54, 2830−2837

Sigma-Aldrich and used as received. The supporting electrolyte $[^nPr_4N][B(3,5\text{-}(CF_3)_2\text{-}C_6H_3)_4]$ was prepared according to literature procedures.[39] Compounds **1**, **2**, $Ce(omtaa)_2$, and $Ce(OQ)_4$ were also prepared following reported procedures.[12,32,33]

Synthetic Details and Characterization. *General Procedure for the Synthesis of 1-X Complexes.* A solution (10 mL) of $Ce[N(SiMe_3)_2]_3$ (0.20 g, 0.32 mmol, 1 equiv) was layered onto a solution (5 mL) of R-2-(^{t}BuNOH)py (3 equiv) and allowed to react at room temperature for 14 h. Red crystals of **1-X** were collected and dried under reduced pressure. The Supporting Information contains specific synthetic details and characterization.

General Procedure for the Synthesis of 2-X Complexes. To a suspension (10 mL) of **1-X** (1 equiv) was added a solution (5 mL) of R-2-(^{t}BuNO•)py formed in situ by the reaction of PbO_2 (18 equiv) and R-2-(^{t}BuNOH)py (3 equiv); the reaction immediately turned dark red to dark purple. Solvents were removed under vacuum after 14 h; excess R-2-(^{t}BuNO•)py was washed away, and the resulting dark powder was dried under reduced pressure. The Supporting Information contains specific synthetic details and characterization.

■ ASSOCIATED CONTENT

Supporting Information

Synthetic details and characterization of the complexes generated, X-ray crystallographic files (CIFs), computational details, ^{1}H NMR data, and electrochemical data. This material is available free of charge via the Internet at http://pubs.acs.org.

■ AUTHOR INFORMATION

Corresponding Author

*E-mail: schelter@sas.upenn.edu.

Notes

The authors declare no competing financial interest.

■ ACKNOWLEDGMENTS

E.J.S. acknowledges the U.S. Department of Energy, Office of Science, Early Career Research Program (Grant DE-SC0006518), the Research Corporation for Science Advancement (Cottrell Scholar Award to E.J.S.), and the University of Pennsylvania for financial support of this work. This work used the Extreme Science and Engineering Discovery Environment (XSEDE), which is supported by the National Science Foundation Grant OCI-1053575. Portions of this work were supported by the Director, Office of Science (OS), Office of Basic Energy Sciences, of the U.S. Department of Energy (DOE) under Contract No. DE-AC02-05CH11231 and were carried out at SSRL, a Directorate of SLAC National Accelerator Laboratory and an OS user facility operated for the DOE OS by Stanford University.

■ REFERENCES

(1) Nugent, L. J.; Baybarz, R. D.; Burnett, J. L.; Ryan, J. L. *J. Inorg. Nucl. Chem.* **1971**, *33*, 2503−2530.

(2) Mamontov, E.; Egami, T. *J. Phys. Chem. Solids* **2000**, *61*, 1345−1356.

(3) Kim, C. K.; Kim, T.; Choi, I.-Y.; Soh, M.; Kim, D.; Kim, Y.-J.; Jang, H.; Yang, H.-S.; Kim, J. Y.; Park, H.-K.; Park, S. P.; Park, S.; Yu, T.; Yoon, B.-W.; Lee, S.-H.; Hyeon, T. *Angew. Chem., Int. Ed.* **2012**, *51*, 11039−11043.

(4) Nair, V.; Deepthi, A. *Chem. Rev.* **2007**, *107*, 1862−1891.

(5) Hong, D.; Murakami, M.; Yamada, Y.; Fukuzumi, S. *Energy Environ. Sci.* **2012**, *5*, 5708−5716.

(6) Wasylenko, D. J.; Ganesamoorthy, C.; Henderson, M. A.; Berlinguette, C. P. *Inorg. Chem.* **2011**, *50*, 3662−3672.

(7) Lee, H. B.; Bogart, J. A.; Carroll, P. J.; Schelter, E. J. *Chem. Commun.* **2014**, *50*, 5361−5363.

(8) Cotton, S. Lanthanide and Actinide Chemistry. In *Lanthanide and Actinide Chemistry*; John Wiley & Sons Inc.: Hoboken, NJ, 2006.

(9) Gupta, C. K.; Krishnamurthy, N. *Int. Mater. Rev.* **1992**, *37*, 197−248.

(10) Piro, N. A.; Robinson, J. R.; Walsh, P. J.; Schelter, E. J. *Coord. Chem. Rev.* **2014**, *260*, 21−36.

(11) Bogart, J. A.; Lewis, A. J.; Schelter, E. J. *Chem.—Eur. J.* **2015**, *21*, 1743−1748.

(12) Bogart, J. A.; Lewis, A. J.; Medling, S. A.; Piro, N. A.; Carroll, P. J.; Booth, C. H.; Schelter, E. J. *Inorg. Chem.* **2013**, *52*, 11600−11607.

(13) Bogart, J. A.; Lee, H. B.; Boreen, M. A.; Jun, M.; Schelter, E. J. *J. Org. Chem.* **2013**, *78*, 6344−6349.

(14) Hansch, C.; Leo, A.; Taft, R. W. *Chem. Rev.* **1991**, *91*, 165−195.

(15) Williams, U. J.; Schneider, D.; Dorfner, W. L.; Maichle-Mossmer, C.; Carroll, P. J.; Anwander, R.; Schelter, E. J. *Dalton Trans.* **2014**, *43*, 16197−16206.

(16) MacDonald, M. R.; Bates, J. E.; Ziller, J. W.; Furche, F.; Evans, W. J. *J. Am. Chem. Soc.* **2013**, *135*, 9857−9868.

(17) Kotani, A.; Jo, T.; Parlebas, J. C. *Adv. Phys.* **1988**, *37*, 37−85.

(18) Isago, H.; Shimoda, M. *Chem. Lett.* **1992**, *21*, 147−150.

(19) Booth, C. H.; Walter, M. D.; Daniel, M.; Lukens, W. W.; Andersen, R. A. *Phys. Rev. Lett.* **2005**, *95*, 267202.

(20) Lukens, W. W.; Magnani, N.; Booth, C. H. *Inorg. Chem.* **2012**, *51*, 10105−10110.

(21) Walter, M. D.; Booth, C. H.; Lukens, W. W.; Andersen, R. A. *Organometallics* **2009**, *28*, 698−707.

(22) Streitwieser, A.; Kinsley, S. A.; Rigsbee, J. T.; Fragala, I. L.; Ciliberto, E. *J. Am. Chem. Soc.* **1985**, *107*, 7786−7788.

(23) Zheng, H.; Yoo, S. J.; Münck, E.; Que, L. *J. Am. Chem. Soc.* **2000**, *122*, 3789−3790.

(24) Behrsing, T.; Bond, A. M.; Deacon, G. B.; Forsyth, C. M.; Forsyth, M.; Kamble, K. J.; Skelton, B. W.; White, A. H. *Inorg. Chim. Acta* **2003**, *352*, 229−237.

(25) Wester, D. W.; Palenik, G. J.; Palenik, R. C. *Inorg. Chem.* **1985**, *24*, 4435−4437.

(26) Streitwieser, A.; Kinsley, S. A.; Jenson, C. H.; Rigsbee, J. T. *Organometallics* **2004**, *23*, 5169−5175.

(27) Elkechai, A.; Mani, Y.; Boucekkine, A.; Ephritikhine, M. *Inorg. Chem.* **2012**, *51*, 6943−6952.

(28) Marenich, A. V.; Ho, J.; Coote, M. L.; Cramer, C. J.; Truhlar, D. G. *Phys. Chem. Chem. Phys.* **2014**, *16*, 15068−15106.

(29) Konezny, S. J.; Doherty, M. D.; Luca, O. R.; Crabtree, R. H.; Soloveichik, G. L.; Batista, V. S. *J. Phys. Chem. C* **2012**, *116*, 6349−6356.

(30) Cui, J.; Hope, G. A.; Buckley, A. N. *Miner. Eng.* **2012**, *36−38*, 91−99.

(31) Pradip; Fuerstenau, D. W. Beneficiation of ores containing rare earth minerals with hydroxamate collectors. *Adv. Sci. Technol. Miner. Benefic. India, Proc. Symp.*; **1983**; pp 217−228.

(32) Williams, U. J.; Mahoney, B. D.; Lewis, A. J.; DeGregorio, P. T.; Carroll, P. J.; Schelter, E. J. *Inorg. Chem.* **2013**, *52*, 4142−4144.

(33) Li, L.; Yuan, F.; Li, T.; Zhou, Y.; Zhang, M. *Inorg. Chim. Acta* **2013**, *397*, 69−74.

(34) Woodruff, D. N.; Winpenny, R. E. P.; Layfield, R. A. *Chem. Rev.* **2013**, *113*, 5110−5148.

(35) Shibasaki, M.; Yamada, K.-I.; Yoshikawa, N. Lanthanide Lewis Acids Catalysis. In *Lewis Acids in Organic Synthesis*; Wiley-VCH Verlag GmbH: Weinheim, Germany, 2008; pp 911−944.

(36) Procter, D. J.; Flowers, R. A.; Skrydstrup, T. *Organic Synthesis using Samarium Diiodide: A Practical Guide*. Royal Society of Chemistry: Cambridge, U.K., 2010; pp FP001−FP204.

(37) Siriwardena-Mahanama, B.; Allen, M. *Molecules* **2013**, *18*, 9352−9381.

DOI: 10.1021/ic503000z
Inorg. Chem. 2015, 54, 2830−2837

(38) Huang, C.-H.; Morrow, J. R. *Inorg. Chem.* **2009**, *48*, 7237−7243.
(39) Thomson, R. K.; Scott, B. L.; Morris, D. E.; Kiplinger, J. L. *C. R. Chim.* **2010**, *13*, 790−802.
(40) *SAINT*; Bruker AXS Inc.: Madison, WI, 2009.
(41) *SHELXTL*; Bruker AXS Inc.: Madison, WI, 2009.
(42) Sheldrick, G. M. *TWINABS*; University of Göttingen: Göttingen, Germany, 2008.
(43) Sheldrick, G. M. *SADABS*; University of Göttingen: Göttingen, Germany, 2007.
(44) Sheldrick, G. *Acta Crystallogr., Sect. A* **2008**, *64*, 112−122.
(45) Booth, C. H.; Walter, M. D.; Kazhdan, D.; Hu, Y.-J.; Lukens, W. W.; Bauer, E. D.; Maron, L.; Eisenstein, O.; Andersen, R. A. *J. Am. Chem. Soc.* **2009**, *131*, 6480−6491.

DOI: 10.1021/ic503000z
Inorg. Chem. 2015, 54, 2830−2837